Mónica Isabel de Abreu Machado

Licenciada em Micro e Nanotecnologias

Laser induced/scribed graphene electrodes for all-printed transistors

Dissertação para obtenção do Grau de Mestre em
Engenharia de Micro e Nanotecnologias

Orientador: Dra. Elvira Maria Correia Fortunato,prof.Catedrática, FCT-UNL

Co-orientadores: Dr. Luís Miguel Nunes Pereira, prof.Associado, FCT-UNL

Júri:

Presidente: Dr.Rodrigo Ferrão Paiva Martins, prof.Catedrático, FCT-UNL

Arguente: Dr. Pedro Miguel Cândido Barquinha, , prof.Auxiliar, FCT-UNL

FACULDADE DE CIÊNCIAS E TECNOLOGIA
UNIVERSIDADE NOVA DE LISBOA

Setembro 2017

Laser induced/scribed graphene electrodes for all printed transistors

ACKNOWLEDGEMENTS

Firstly, thanks to professor Rodrigo Martins for the assembly of this breakthrough master degree, professor Elvira Fortunato and professor Luís Pereira for allowing me to do research in this excellence center, which is CENIMAT.

My deep and sincere gratitude also goes to Carolina Marques, Ana Samouco, João Ferrão, Inês Cunha, Tiago Carvalho, Paul Grey, Cristina Gaspar, Rodrigo Santos, Beatriz Coelho, Joana Cerdeira, Sónia Pereira, Alexandra Gonçalves and all the people who shared the openspace with me.

Without a great education nothing is possible, so I would like to thank all the nuns and teachers of Externato da Apresentação de Maria. I also would also like thank the best math teachers in the world, Alberto Ferreira and Gertrudes Abreu.

To my best friends, Gabriel Marcelino, Raquel Almeida, Felipe Torrado, Ricardo Rodrigues, Catarina Mouzelo, Jakelyn de Jesús, Jorge Emídio, thank you for not letting me give up.

I dedicate this work to two great men which were gone too soon, Abel Porfírio de Abreu and Carlos Machado and to my parents.

ABSTRACT

This work reports the development of electrolyte gated transistors (EGTs) whose source, drain and gate electrodes are made of laser induced graphene (LIG) on polyamide (PI). The direct patterning of such electrodes with an intended application for EGTs has never been accomplished before.

LIG was characterized using a scanning electron microscope (SEM) and Raman Spectroscopy. The minimum sheet resistance achieved with this laser method was 24 Ω/sq.

Two types of staggered bottom gate transistors were printed, one using a reusable hydrogel sticker electrolyte and the other using a liquid electrolyte, tetramethylammonium hydrogen phthalate. A semiconducting ink based on a dispersion of zinc oxide nanoparticles (ZnO) on ethyl cellulose (EC) was screen-printed on the PI substrate. Electrochemical Impedance Spectroscopy (EIS) and cyclic voltammetry (CV) was performed with the intent to evaluate the electric double layer (EDL) formation on EGTs. e. The ZnO EGts present some electrical modulation with On/Off ratios orders of 10^2, transconductance orders of 10^5 S and saturation mobilities (μ_{sat}) orders estimated at 10^{-3} $cm^{-2}(Vs)^{-1}$.

Keywords: laser induced graphene, polyamide, electrolyte-gated transistor

.

RESUMO

Este trabalho reporta o desenvolvimento de *electrolyte-gated* transístores (EGT) cujos contactos de fonte, dreno e porta foram obtidos por indução a laser de grafeno em poliamida. A padronização destes electródos com vista a aplicação em eletrónica flexível nunca foi testada previamente.

Os elétrodos obtidos com este método foram caracterizados através de microscopia eletrónica de varrimento (SEM) e espectroscopia *Raman*. A resistência folha mínima atingida com este método foi de 24 Ω·cm.

Dois tipos diferentes de *staggered bottom gate* transístores foram impressos com diferentes eletrólitos, um deles com um composto celulósico reutilizável e outro com um eletrólito líquido, nomeadamente ftalato tetra metilo hidrogénio. Uma tinta semicondutora base numa dispersão de nanopartículas em etilo celulose (EC) foi impressa no substrato de poliamida mediante o uso da técnica de *screen-printing*. A espectroscopia de impedância eletroquímica (EIS) e a voltametria cíclica foram as técnicas utilizadas para avaliar a formação de uma dupla camada eléctrica. Os ZnO NPs EGTs apresentaram alguma modulação elétrica para e em termos de propriedades elétricas apresentaram razões On/Off na ordem de 10^2, mobilidade de saturação (μ_{Sat}) na ordem de 10^{-3} $cm^{-2}(Vs)^{-1}$ e transcondutância (g_m) na ordem de 10^{-5} S.

Palavras-chave: laser, indução, poliamida, grafeno, *electrolyte-gated transistor,*

LIST OF ABBREVIATIONS

a.u – Arbitrary units

AC – Alternating current

CENIMAT|i3N – Centro de Investigação de Materiais|Instituto de Nanoestruturas, Nanomodelação e Nanofabricação

CHE – Composite Hydrogel Electrolyte

CPE – Constant phase element

CSPE –Composite solid polymer electrolyte

CV – Cyclic voltammetry

CVD – Chemical Vapor Deposition

DC – Direct current

EC – Ethyl cellulose

ECM – Equivalent circuit model

EDL – Electric double-layer

EDLC – Electric Double Layer Capacitor

EGT – Electrolyte-gated transistor

EIS – Electrochemical impedance spectroscopy

FET – Field-effect transistor

GO – Graphene Oxide

NPs – Nanoparticles

PBI – Polybenzimidazole

PET – Polyethylene terephthalate

PI – Polyamide

rpm – Revolutions per minute

RT – Room temperature

TMAHP – Tetramethyl ammonium hydrogen phthalate

TFT – Thin film transistor

UV – Ultra-violet

LIST OF SYMBOLS

A – Ampere

C– Capacitance

C_b – Electrolyte bulk capacitance

C_{DL} – Capacitance of electric double-layer

C_i – Capacitance of the dielectric layer

CO_2 – Carbon dioxide

D – Distance

F – Farad

f – Frequency

g_m – Transconductance

Hz – Hertz

Im (Z) – Imaginary part of impedance

I_{DS}– Drain current

I_{GS} – Gate leakage current

L – Channel length

m – Meter

k- effective dielectric constant

R_b – Electrolyte bulk resistance

R_{CT}– Charge transfer resistance

Re(Z) – Real part of impedance

R_{ext} – Exterior contact resistance

R_s – Sheet resistance

S – Siemens

S_s – Subthreshold swing

s – Second

t- thickness

V - Volt

V_{DS} – Voltage between drain and source

V_{GS} – Voltage between gate and source

V_{On} – Turn-on voltage

V_{Th} – Threshold voltage

W – Channel width

Y_0 – Capacitance of a constant phase element

Z – Impedance

σ_i – Ionic conductivity

α – Fractal surface character

μ_{Sat} – Saturation mobility

μ_{FE} –Field-effect mobility

ρ – Electrical bulk resistivity

Ω – Ohm

°**C** – Degrees Celsius

$\boldsymbol{\varepsilon_0}$ –Dielectric permittivity

$\boldsymbol{\varepsilon_i}$ –Dielectric constant of an insulator

$\boldsymbol{\lambda}$ –Debbie screening length

TABLE OF CONTENTS

LIST OF FIGURES

LIST OF TABLES

1 MOTIVATION AND OBJECTIVES

1.1 Motivation

In the early nineties Mark Wieser introduced the concept of Ubiquitous Computing. According to his point of view, instead of an interface centered interaction, computing should be incorporated naturally with human behavior and everyday objects. This concept should become a reality with the rise of Internet of Things (IoT) if most objects become interconnected wirelessly.[1]

Microelectronic fabrication processes should also diverge from conventional ones so they can become compatible with a plethora of materials. Different techniques have been proposed such as screen-, flexo-, gravure-, offset- and inkjet printing. These present several advantages, among them, the possibility of a high throughput by substituting complex and subtractive processes for cheaper and simultaneously environmentally friendlier ones applicable in roll to roll fabrication. [2]–[5]

Within this broad topic, the focus of this work will be on laser induced/scribed graphene electrodes on flexible substrates for all printed electrolyte gated transistors (EGTs). The successful fabrication of such electrodes for in-plane microsupercapacitors has already been reported in literature.[6]–[14]. EDLs are responsible for the high capacitances reported on graphene microsupercapacitors so the same principles could be applied on EGT fabrication. EGTs, besides being printable, work with low voltages due to the high capacitance provided by the formation of an electric double layer (EDL) on the interfaces in contact with the electrolyte.[15]. These could also play a role in the demand for biosensing applications since the drain current is influenced by any physical or chemical modification of the EDL.[16]

.

1.2 Objectives

The main purpose of this dissertation is to design, fabricate and characterize electrolyte gated transistors combining laser induced/scribed graphene electrodes with screen printed zinc oxide nanoparticles (ZnO) in ethyl cellulose as the semiconductor material. Two different electrolytes will be tested, a reusable cellulose based hydrogel sticker film [17] and tetramethylammonium hydrogen phthalate (TMAHP).

Therefore, the following aspects on this study will be covered:

- Optimization and characterization of laser induced/scribed graphene electrodes
- Study of graphene electrodes influence on double-layer capacitance with cyclic voltammetry (CV) and Electrochemical Impedance Spectroscopy (EIS)
- Electrical characterization of EGTs

2 INTRODUCTION

2.1 Microsupercapacitors and EGTs

Conventional capacitors consist of two conducting electrodes separated by an insulating dielectric material. When a large enough voltage is applied, opposite charges accumulate on the surfaces of each electrode and are kept separate by the dielectric material. For these capacitors, capacitance, C is directly proportional to the surface area A of each electrode and inversely proportional to the distance D between electrodes, ε_O is the dielectric constant of "free space" or permittivity between the two electrodes and ε_i is the dielectric constant of the insulating material (Equation 1). The same principles are applied to supercapacitors; however, the difference lies on a much larger surface area A and much thinner dielectrics (molecule size).[18] As voltage is applied and charge accumulates on electrode surfaces, ions in the electrolyte solution diffuse across the separator pores into the pores of the electrode with opposite charge forming the double layer. Charge storage is then highly reversible.[18] Taking this into consideration, in 1853 a model was proposed by Helmholtz (Equation 1) where the differential capacitance was proportional to ε_0 and k (the effective dielectric constant of the EDL) and inversional to λ, the Debbie screening length.[15]

$$C = \varepsilon_i \varepsilon_0 \frac{A}{D} = \frac{k\varepsilon_0}{\lambda} \quad (1)$$

The fundamental characteristic of field effect transistors (FET) is the modulation of current flow between two electrodes (source and drain, I_{DS}) by applying a voltage on a third electrode, the gate (V_{GS}). The dielectric insertion between the semiconductor and the transversal gate electrode injects carriers capacitively close to the dielectric/semiconductor interface, known as the field-effect. [19] The induced charges by V_{GS} are collected by the drain electrode (in the case of a n-type FET). Thin film transistors (TFTs) differentiate from MOSFETs mainly because different fabrication processes are used instead of diffusion, implantation processes in silicon wafers. The use of electrolytes instead of conventional dielectric layer as in FETs results on a EGTs.[20], [21].

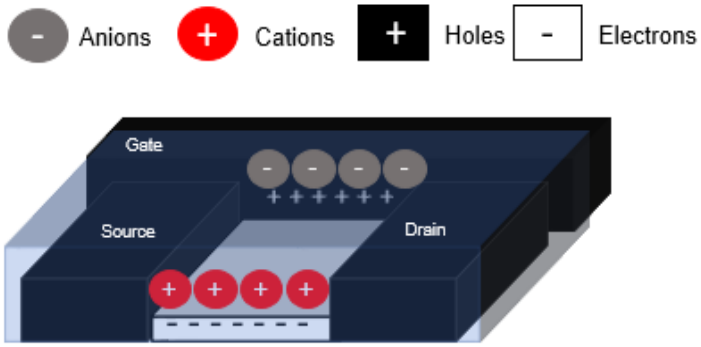

Figure 2.1 Schematic representation of the staggered bottom-gate structure

There are two basic operation mechanisms for EGTs. One in the case where the semiconductor is impermeable to ions of the electrolyte and the other when it is permeable. For impermeable semiconductors (Figure 2.1 Schematic representation of the staggered bottom-gate structure), when voltage is applied to the gate, migration and accumulation of charges is seen at gate-electrolyte and

semiconductor-electrolyte interfaces. Ideally the charge accumulation process is reversible and the transistor returns to its neutral state upon removal of the gate bias, responsible for the driving forces of ion migration. With permeable semiconductors, an EDL may be formed at the gate/ electrolyte interface upon application of a gate voltage, but ions on the semiconductor-electrolyte interface diffuse into the semiconductor film and compensate induced charged carriers by source and drain electrodes.[15]

The evolution from conventional dielectric materials (oxides and nitrates) to electrolytes was governed by the need for higher transistor driving currents, since it is directly proportional to the capacitance of the dielectric layer per unit area (C_i). Electrolytes can reach values in the order of 1–10 μFcm^{-2}, outperforming even high-k dielectrics. As we can see in Equation 2 where W and L are the channel width and length respectively, μ_{FE} the field effect mobility, V_G, V_T, V_D are the gate, threshold and drain voltages respectively. For a given μ_{FE}, a larger capacitance means that the same I_D could be obtained at lower V_G and V_D.

$$I_D = \frac{w\mu_{FE}\, c_i}{L}\left[(V_G - V_T)V_D - \frac{V_D^2}{2}\right] \quad (2)$$

A considerable drawback in EGTs employment remains in their significant gate leakage currents (I_{GS}), arising from considerable charging currents of the ion accumulation process and high parasitic capacitances, limiting the expected increase of the drive current. [15]

2.2 Graphene

Porous carbon materials such as activated carbon, xerogels, carbon nanotubes, mesoporous carbon and carbide derived carbons have been investigated for their use as electrodes in electrical double layer capacitors (EDLCs). [22] Since its isolation and proof of existence in 2004 by Noselov et. al, graphene has still not entered mass production due to synthesis complexity, high costs, low yields and compromises in purity as shown on Table 2.1.The commercial interest in graphene relies on its unique properties such as a maximum electron mobility of $2{,}5\times10^5$ $cm^2\ V^{-1}\ s^{-1}$ (with a simultaneous ability to sustain high current density), chemical inertness, high thermal conductivity, super hydrophobicity and a Young modulus of 1 TPa.[23], [24]

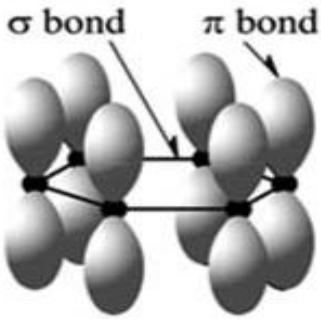

Figure 2.2 Schematic representation of graphene structure adapted from [24]

Graphene is a 2D allotrope of carbon, formed by a hexagonal lattice. As a sp^2 hybridized material, s, p_x, and p_y atomic orbitals on each carbon hybridize to form strong covalent bonds, giving rise to 120° C-C-C bond angles. The remaining p_z orbital on each carbon overlaps with its three neighboring carbons to form a band of filled π orbitals, known as the valence band, and a band of empty π* orbitals, called the conduction band. With no chemical bonding in the c-direction, out-of-plane interactions are extremely weak. This includes the propagation of charge which leads to out-of-plane electrical conductivities. A lot

of research has been done for graphene as zero band gap and ambipolar semiconductor in transistors but this is not the aim of the present study.[25] Bi-layer and few-layer graphene is proved to behave more like a metal, especially with the increase in the number of layers presenting still a surface area comparable to that of monolayer graphene.[24] Due to the properties mentioned above, multi-layer graphene is an ideal candidate for source, drain and gate electrodes in flexible printable electronics.

Table 2.1 Comparison of different methods used in graphene synthesis [26]

Method	Thickness	Advantage	Disadvantage
Confined self-assembly	Single layer	Thickness control	Defects
Chemical vapor deposition (CVD)	Few layer	Large size, high quality	Small production scale
Arc discharge	Single, bi and few layers	10g/h graphene production	Low yield of graphene, carbonaceous impurities
Epitaxial growth on SiC	Few layers	Very large area of pure graphene	Very small scale
Unzipping of nanotubes	Multiple layers	Size controlled by the selection of the starting nanotubes	Expensive starting material, oxidized graphene
Reduction of graphite oxide	Multiple layers	Un-oxidized sheets	Contamination
Micromechanical exfoliation	Few layers	Large size and unmodified graphene sheets	Very small scale production
Direct sonication of graphite	Single and multiple layers	Unmodified graphene, inexpensive	Low yield, separation
Electrochemical exfoliation/functionalization of graphene	Single and few layers	Single step and high electrical conductivity	Cost of ion liquids
Super acid dissolution of graphite	Mostly single layer	Unmodified graphene, scalable	Use of hazardous chlorosulfonic acid, cost of acid removal

2.3 Zinc Oxide

The interest in zinc oxide (ZnO) was enhanced after 2003 when good performing devices showing that oxide semiconductor-based TFTs could be a viable technology, with the reports on TFTs by Hoffman et al, Carcia et al.and Masuda et al. [27]–[29]. Also, ZnO meets many requirements simultaneously, it is environmentally friendly, non-toxic, low-cost and can be prepared on a large scale by following inexpensive synthesis routes.[30]. Some important achievements were the enhanced device performance (mainly regarding mobility) at room temperature processing and non-vacuum processes to produce ZnO layers.[19], [31]–[33]. Concerning solution based ZnO production, different techniques have been proposed

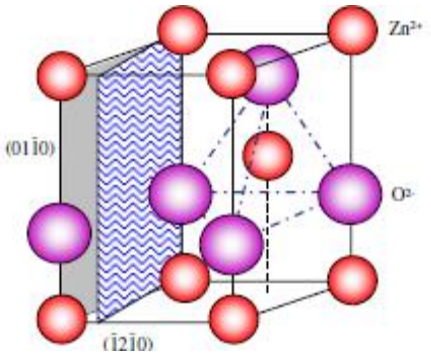

Figure 2.3 Zinc crystalline structure adapted from [39]

although an annealing step is usually needed. Spin-coating[16] [34]–[36], spray pyrolysis [37], aerosol jets [38] are some of the techniques that showed promising results.

ZnO is a wide band gap (3.37 eV) compound n-type semiconductor with high binding energy (60 meV) and high thermal and mechanical stability making it attractive for potential use in electronics.[39] In materials science, zinc oxide is classified as a semiconductor in group II-VI, whose covalence (sp^3) is on the boundary between ionic and covalent semiconductors. The most common crystalline phase at ambient conditions is hexagonal wurtzite represented on Figure 2.3 where each anion is surrounded by four cations at the corners of a tetrahedron and vice-versa.[40]

There has been an intense debate about the n-type intrinsic nature of ZnO crystals. None of the native defects exhibits characteristics consistent with a high-concentration of shallow donors. Only vacancies have sufficiently low energies to form during synthesis of the material, but zinc vacancies behave as deep acceptors and oxygen vacancies as deep donors. The prevailing n-type conductivity can therefore not be attributed to native defects; it must thus be caused by impurities that are unintentionally incorporated. Since zinc oxide processing highly influences the outcome product, the incorporated impurities can enhance or diminish n-type conductivity. The previous results reported in literature could be related with the unintentional incorporation of impurities that act as shallow donors. A common impurity present in most processes is hydrogen. The amphoteric behavior of interstitial hydrogen seen in most semiconductors is not verified in ZnO as in most common semiconductors, instead it forms a strong bond with oxygen and acts as a shallow donor. However, this phenomenon does not explain the high conductivity at relatively high temperatures but provides a good explanation for the relatively high conductivities obtained through room temperature processes. Another suggested common bond is the interstitial one where H can also substitute for oxygen in ZnO and act as a shallow donor as well. Substitutional H is much more stable than interstitial H and can explain the stability of the n-type conductivity at high temperatures and its variation with oxygen partial pressure.[41]–[43]

Several functional printable EGTs based on solution processed ZnO have been reported and the obtained values from electrical characterization are summarized on Table 2.2.

Table 2.2 Key parameters of the reported EGTs where ZnO was implemented

Ref.	**Deposition Technique**	**Post-treatment**	**Electrolyte**	**V_T (V)**	**ON/OFF**	**μ ($cm^2(Vs)^{-1}$)**
[38]	Aerosol Jet Printing (AJP)	250ºC	Ion-gel ink	0.97	2.15×10^5	1.61
[16]	Spin-coating	450ºC	aqueous electrolyte	0.57	~10^3	0.81
[36]	Spin-coating	150ºC	Ion-gel	0.7	~10^5	13

2.3.1 Laser induced/scribed graphene

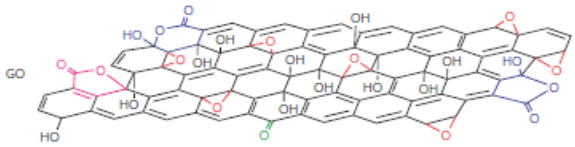

Figure 2.4 Schematic representation of graphene oxide adapted from [6]

Graphite by itself is highly hydrophobic and so its dissolution and exfoliation is facilitated by oxidation. Graphene oxide (Figure 2.4) has attracted some attention due to its scalability, low cost and wet chemical approach to graphene fabrication The conductivity of graphene oxide (GO) is dominated by ionic conductivity, depending on environment and varies between 5×10^{-6} S cm^{-1} and 4×10^{-3} S cm^{-1}, closer to an insulating behavior .[6] To obtain the desired electrical properties of graphene, a reduction step is needed which frequently involved hazardous chemicals such as hydrazine or high annealing temperatures.[7] In 2010, graphene oxide reduction was successfully achieved by laser with a femtosecond laser [45] and an atomic force microscope (AFM) tip[46]. In 2011, an important breakthrough was the direct laser writing of graphene for in plane microsupercapacitors on a CO_2 laser system.[6] Following the same principle, several microsupercapacitors were built in the last years using light scribe technology proving that laser incident energy on the order of mW is sufficient to decrease sheet resistance up to 80Ω/sq.[7], [47]–[50] The mechanism behind reduction is a laser incident energy higher than the binding energies (285-289 eV) of the characteristic functional bonds of graphene oxide, carboxyl, sp^3 carbons in the form of epoxide and hydroxyl carbons, leading to a decreased content in oxygen and restoration of sp^2 hybridization which translates into lower sheet resistances. [48]

Another topic of research has been the carbonization of polymers by lasers. In 1991, a reported carbonization of polyimide (PI) and Polybenzimidazole (PBI) with ultraviolet radiation produced highly conductive structures with a resistivity on the order of 1-10 Ω cm^{-1} but the nature of this resistivity was unknown.[51]. Later on, few-layered graphene was obtained by brief pyrolysis of vinyl polymers at 1000ºC during 1 minute under a 50 nm thick capping layer. It was theorized that graphene formation was due to the bond cleavage of volatile species and posterior cyclization of C-C bonds under the capping layer. [52] Recently, the irradiation of PI sheets has produced carbonized structures denominated laser induced graphene (LIG). LIG formation is most likely caused by photothermal effects owing to the long wavelength (~10,6 µm) and relatively long pulses (~14 µs) of the CO_2 laser. The energy from laser irradiation results in lattice vibrations which could lead to extremely high localized temperatures(>2500ºC). These high temperatures easily break C-O, and N-C bonds. The occurrence of cyclization is attributed to the minimized oxidation due to the over layer of evolved gases. [11] The synthesized electrodes via this route render enhanced accessible surface areas and facilitate electrolyte penetration into the active materials. Numerous microsupercapacitors have also been reported in literature with this technique.[11], [13], [53]

2.4 Printed electronics and Printing Techniques

Printed Electronics promises to revolutionize the existing electronics field by enabling the mass production of low-cost, flexible digital devices in a wide array of substrates, such as paper, plastic or textiles. The drive for printed electronics is also highly based on the use of purely additive maskless

processes. Not only the material could be deposited when required but also, the overall complexity is reduced because typically only two steps are required, the printing and curing steps. Therefore, an optimization of both steps is required for cost savings. Unfortunately, there is a trade off since printing components still do not present the quality performances of their non-printed counterparts. Hence printed electronics is not perceived as substitution of common silicon based-technology but as an opportunity for different technologies and markets.[1]

Processing steps with long sintering times (>30 min) or high temperatures (>250ºC) are not advantageous for large scale printing. As an illustrative example, a sintering time of 30 minutes with web speeds of 1 m/s means that the production length is required to be at least 1.8 km in length. Additionally, high sintering temperatures are not compatible with polymers like PET which have relatively low glass transition temperatures (T_g). Room temperature sintering can be done in a couple of ways. One way simply allows the solvent to evaporate slowly which causes the stabilizer to collapse onto the particles surfaces followed by nanoparticle coalescence. Another common method has been UV radiation which causes chemical reduction.[2] . A summary of the existing techniques is depicted on the organogram on Figure 2.5

The key components of printing electronics are essentially a flexible circuit board to be used as substrate and the use of inks as semiconductors. Polyimide which has a high thermal and chemical resistance is the most widely used flexible substrate. Its use is only limited by its intrinsic color for transparent electronics and cost compared with polyethylene terephthalate (PET).[3]. Stretchable electrodes like graphene with low contact resistance, good adhesion and electrical stability are extremely important in restraining strain induced artifacts during device operation and so, laser induced carbon electrodes on PI present an excellent solution. [44]. Metal oxides inks have been widely used in various devices such field-effect transistors (FETs), and also have the advantage of providing fast film deposition over large areas using simple methods.[3]

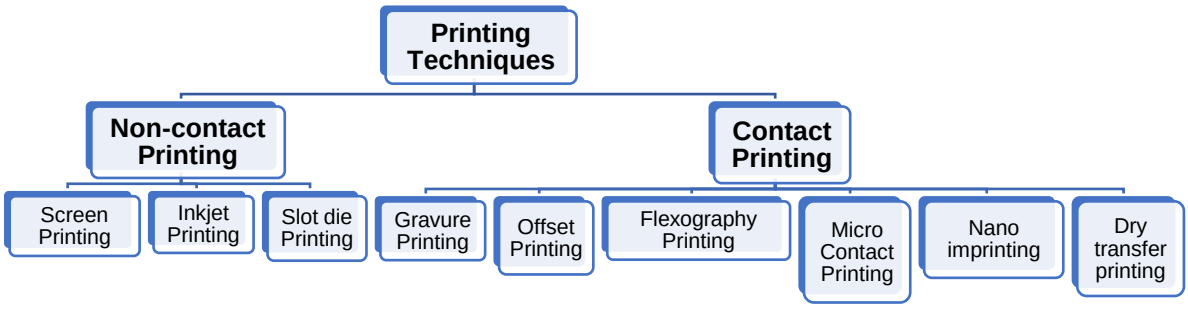

Figure 2.5 Organogram of the existing printing techniques adapted from [4]

2.4.1 Screen-Printing

Screen-Printing was the fabrication technique adopted for the semiconducting layer. It consists of a squeegee, or a metal or a rubber moving over a screen mesh which provides sheer stress to the printable paste/ink decreasing its viscosity and allowing it to cross through the open areas onto the substrate as depicted on Figure 2.6. The printing quality depends on several factors, namely, solution viscosity (500-5000 cPs), printing speed, angle and geometry of the squeegee, mesh size, material, strength, snap off (distance between screen and substrate),substrate and ink surface energies.[54]

Ink formulation plays a major role. A sacrificial binder is often used for the dispersed metal oxide powders to hold the particles together and provide the necessary rheological properties for good printing and levelling. Usually an additional step of “burning out” the vehicle is needed so that conductivity is not impaired.

Resin and polymeric binders, especially cellulose polymeric binders are the preferable choices. Ceramic pastes are typically non-Newtonian fluids, in other words, their viscosity is time and shear dependent due to the formation or breakdown of structural networks of particle-particle or particle-polymer interactions. The presence of a cellulose compound like ethyl cellulose (EC) modifies the rheological behavior of the pastes due to its surface affinity and ability to form hydrogen bonds. Shear thickening by the formation of polymer bridges between particles has already been reported and has a major impact on the quality of the screen printed films. [55]

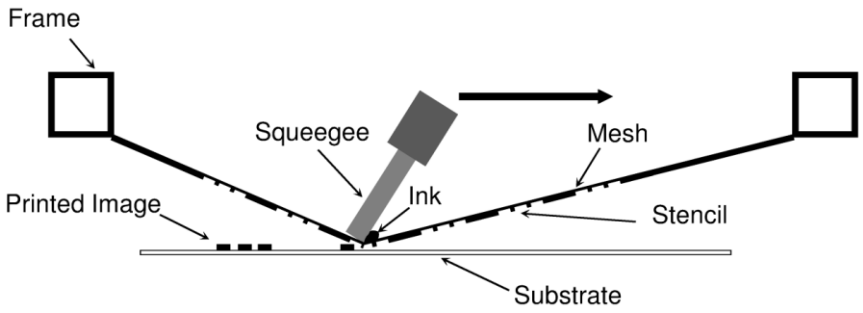

Figure 2.6 Schematic of the screen-printing process adapted from [64]

3 MATERIALS AND METHODS

This chapter aims to present all the steps that were taken for the production and characterization of EGTs.

3.1 Graphene electrodes

Two methods based on literature were used for preparing graphene electrodes, the laser induced method [11] and the laser scribed method [6]. Laser inducing/scribing was conducted on PI and PET sheets respectively with a CO_2 laser cutter system, ~10.6 wavelength (Universal Laser System VLS3.50). To engrave properly with the laser beam, the material must be placed exactly at that focus point which in this case was the maximum z position closest to the beam. The laser software presents three adjustable parameters namely, speed, power and pulses per inch and both power and speed can only by adjusted with 1% step. Also, the laser can work with two different modes, vector cut and raster engraving mode. For the raster engraving mode the maximum speed and power are 1,27 m/s and 50 W. For this laser mode, both DuPont™ Kapton® HN general-purpose film with a 75 µm and 50 µm thickness were used as substrates for laser induced graphene.

Direct carbonization of PI was conducted via laser irradiation. The first tests were done with triplicates of the same conditions on 75 µm PI sheets with lines of 1 cm in length and 300 µm in width separated by 2 mm drawn on Adobe Illustrator. These tests were replicated on 50 µm PI sheets. Laser scribed graphene was obtained with the same laser engraving mode.

Graphene oxide (5 mL) was purchased from Graphenea (0.05 wt% concentration, 0.125 g GO content) and drop casted on 9 cm^2 PET circles and dried on a vacuum desiccator with silica for about 48 hours at ambient temperature. PET was previously exposed to UV radiation for 15 minutes. Direct carbonization of the graphene oxide films was conducted also via laser irradiation. The same tests with triplicates of the same laser parameters were conducted.

3.2 Fabrication of the ZNO NPs ink, formulation, materials and reagents

The method used for the preparation of ZNO NPs screen printed paste was based and adapted from literature. [56] First, the vehicle was prepared by dissolving 5 % wt Ethyl Cellulose 300 cP ($C_6H_7O_2(OC_2H_5)_3$; CAS: 9004-57-3) from Aldrich on an 80:20 toluene/ethanol solution ($C_6H_5CH_3$; CAS: 108-88-3/ C_2H_6O; CAS: 64-17-5). After complete dissolution, which takes around 12 hours under stirring at 600 rpm, a paste with 40% wt ZnO <100 nm particle size (CAS: 1314-13-2) from Aldrich was obtained by adding the solution to the powder. The paste was stirred at 200 rpm for two hours.

3.3 Fabrication of interdigital capacitors

Laser printed electrodes on PI were employed in the fabrication of in plane interdigitated microcapacitors in which LIG served as both the active and current collectors.[11] Silver contacts were added to improve the contact with the potentiostat device and served as negative and positive electrodes. Two different capacitors were fabricated, a capacitor with tetramethylammonium hydrogen phthalate (TMAHP) embedded on a separator membrane (titanium 60l) purchased from KEMET in which the active electrodes were defined with Kapton tape and a reusable sticker electrolyte - cellulose based composite hydrogel electrolyte (CHE) with 2.9 wt% in Li^+ ions. [17]. A schematic representation of the different layers is depicted on Figure 3.1.

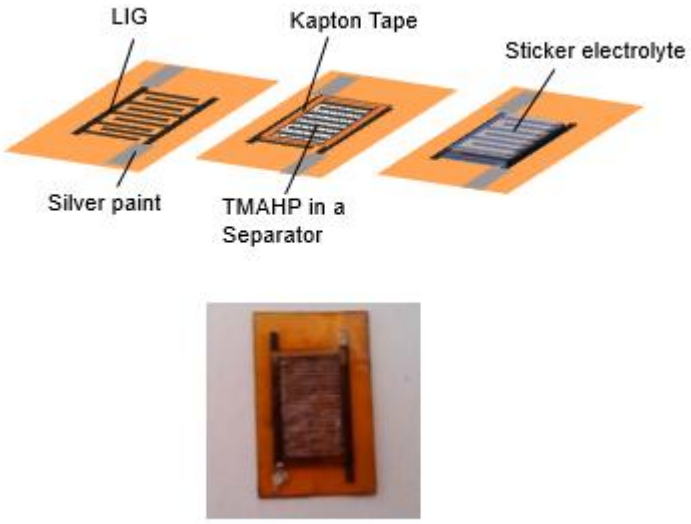

Figure 3.1 Schematic representation of the fabricated microsupercapacitors

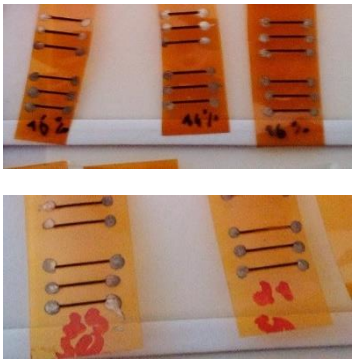

Figure 3.2 Example of LIG samples with silver paint for IV measurements

3.4 Fabrication and optimization of ZNO NPs EGTs

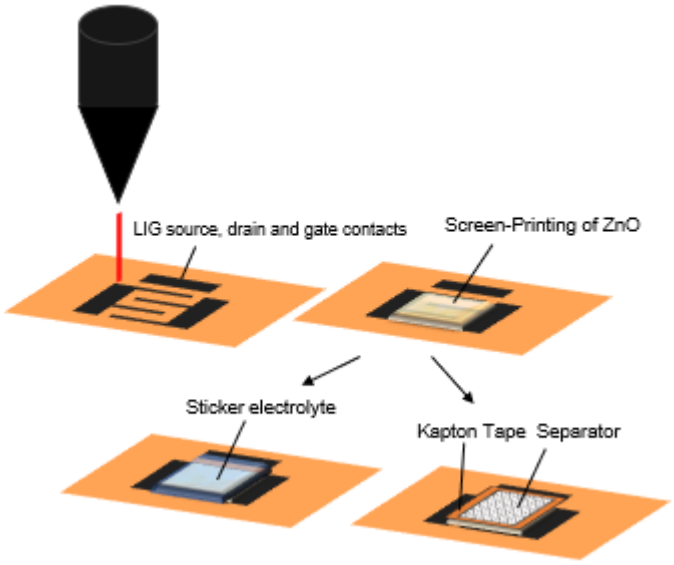

Figure 3.3 Schematic representation of the fully developed EGTs

For of ZnO NPs EGTs, a staggered bottom-gate architecture was adopted. Source, drain and gate electrodes were drawn on Adobe Illustrator and printed by laser induction of graphene on the 75 µm PI substrate. The semiconductor was printed with a mesh model 77-55 (mesh count 190, aperture 81 µm and thread diameter 55 µm). Two different electrolytes were used in the same way as presented above. The schematic representation of both transistors is represented on Figure 3.3.

3.5 Characterization techniques

Several techniques were used for the characterization of graphene electrodes. Two-point IV sweep measurements were done on Agilent 4155c and the exemplification of the samples used are seen above on Figure 3.2. The dimension of graphene electrodes was determined by microscopic observation. The quality of graphene sheets was evaluated through Raman Spectroscopy with Raman Microscope-Renishaw Quontor. Electrode samples were also analyzed with a scanning electron microscope Hitachi TM3030 Tabletop SEM Series. Energy dispersive X-Ray Spectroscopy (EDS) was conducted to investigate the chemical species present.

Electrochemical Impedance Spectroscopy (EIS) and cyclic voltammetry (CV) measurements were done using Gamry Instruments Reference 600 Potentiostat. EIS evaluated the capacitance-frequency dependence of both capacitors. The results were acquired in a frequency range of 1 MHz to 10 mHz with 25 mV as AC excitation voltage at 1 V DC. CV measurements were done to calculate the capacitance of graphene interdigital capacitors with approximate superficial area of 1,83 cm^2 of both electrolytes and investigate about the chemical inertness of graphene electrodes. Also, the electrochemical response of the combination of ZnO NPs ink with the electrolytes was evaluated so that possible redox reactions between the two could be identified.

The electrical characterization of EGTs transistors with the sticker electrolyte was performed in the dark at room temperature using an Agilent 4155C semiconductor parameter analyzer connected to a Cascade Microtech M150 manual microprobe station, controlled by the software Metrics ICS. The electrical characterization of the EGT with TMAHP was performed on a Semiconductor Characterization System (Keithley 4200-SCS).

4 RESULTS AND DISCUSSION

4.1 Characterization and optimization of graphene electrode

In this section, the focus will be on the development and characterization of laser induced/scribed graphene electrodes.

4.1.1 LIG morphological and electrical characterization

Firstly, an overall evaluation of the conditions that led to the carbonization and engraving of PI without polymer ablation was conducted since the conditions for laser induced graphene formation were not known for this laser system. The successfully engraved lines were studied in terms of dimension and resistance. A summary of the test results for a wide range of carbonized engraved lines is represented on the contour plots Figure 4.1.

a) b)

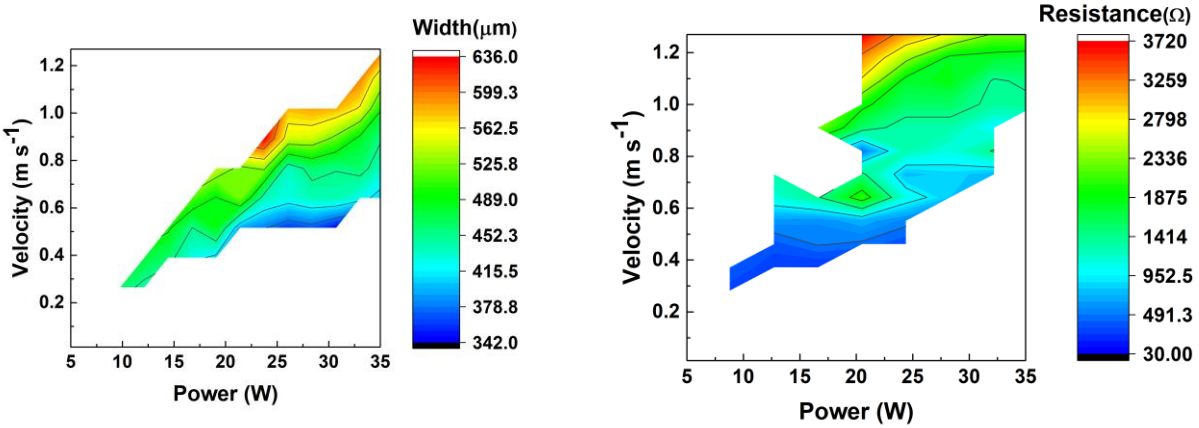

Figure 4.1 a) LIG average width variation at different laser powers and velocities b) LIG resistance variation at different laser powers and velocities

The tests made on 75 µm thick PI for graphene production indicated that in general, increasing power and velocity lead to higher resistances and deviations from the nominal width (300 µm) although it is not a linear correlation, that is, this phenomenon is only observed to a certain extent. Also, the number of engraving parameters becomes more restricted with decreasing laser power and velocity, yet this smaller range induces LIG with lower resistance. A lower velocity is associated with an increased time of the substrate to radiation for each sweep of the laser and that is probably why ablation increases in these conditions but on the other hand, the laser induction is more effective.

A further study including sheet resistance measurements was done in a more restricted range of lower laser power and velocity. Sheet resistance was measured as demonstrated in Equation 3 where R_s stands for sheet resistance, W for width and L for length. The calculated sheet resistances are represented on Figure 4.2.**Erro! A origem da referência não foi encontrada.**

$$R_S = R\frac{W}{L} \tag{3}$$

a) b)

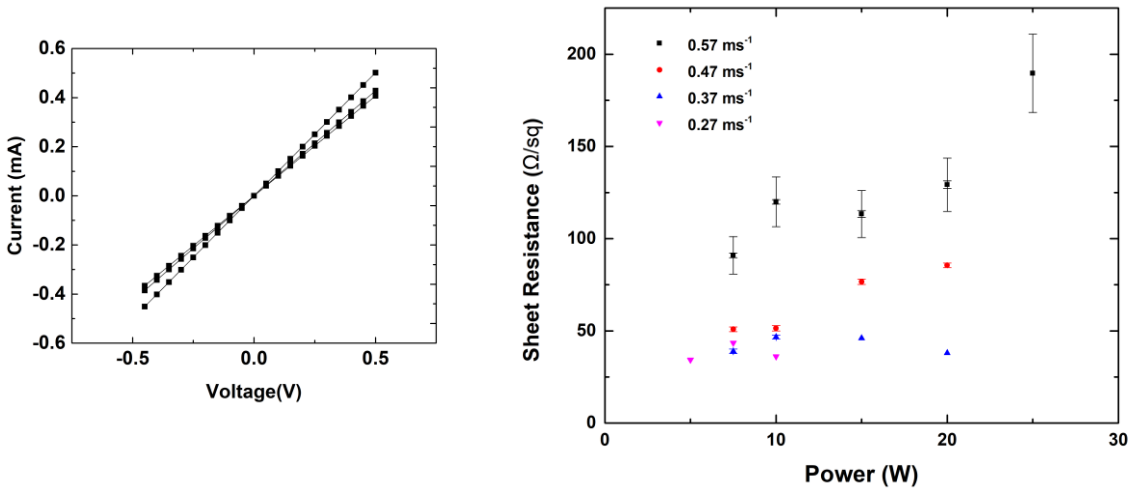

Figure 4.2 a) IV curve of three samples obtained with the same conditions b) LIG sheet resistance from 2.5 to 30 W at different velocities

As it can be observed from the represented graph of sheet resistance, a higher velocity is linked with an increased standard deviation associated with the error propagation of width and resistance. When it comes to lower velocities the standard deviation decreases so much that is not even significant as it can be observed in the graph above on Figure 4.2. A more accurate study in terms of electrical characterization is the resistivity measurement. The thickness of the SEM samples was calculated using image J software and the results are present on Figure 4.3 and Figure 4.4.

Resistivity was calculated using Equation 4 where ρ stands for resistivity, R_S for sheet resistance and t for thickness. The results obtained through this equation are represent on Figure 4.4.

$$\rho = R_S \times t \tag{4}$$

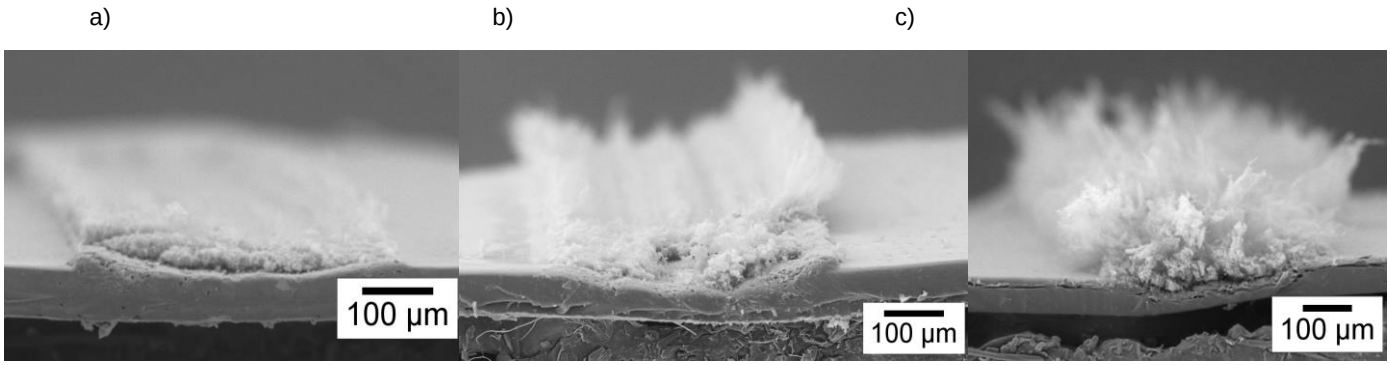

Figure 4.3 SEM images of LIG at a constant velocity (0.29 m s-1) and increasing power a) 15 W b) 15 W c) 20 W

The minimum registered resistivity in the present study was around 0.1 (Ωcm). Since resistivity is an intrinsic property of a material, the values obtained after thickness measurements could be associated with the conversion degree of the polymer into pure carbon, meaning that certain chemical bonds are not efficiently dissociated, especially for higher power and velocity. An increase in power is associated with a partial oxidation of LIG in air. [11] Also, the remaining oxygen and hydrogen atoms could be rearranged with carbon forming nonvolatile compounds Common PI pyrolysis products are certain nonvolatile species benzene, toluene, phenol, etc. [57] In accordance with the obtained results it is possible to observe on Figure 4.3 a more porous and heterogenous material with increasing laser power and speed, characteristic of a rapid superficial sublimation and solidification which confers different properties.

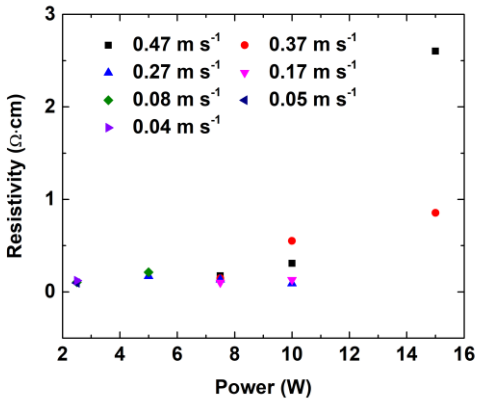

Figure 4.4 LIG resistivity from 2.5 to 15 W at different velocities

After a full morphological and electrical characterization, the interval of parameters for analysis was shortened even more for velocities below 0.17 m s^{-1} and lower power ranges, between 10 and 7 W. The most reproducible results and with lower standard deviations are depicted on Figure 4.5.

Considering the optimized sheet resistance of 23.7 Ω/sq achieved at a velocity of approximate 0.14 m/s and 7 W of laser power, this result is coherent with the first reported values on literature which indicated that the lowest sheet resistance possible with the proposed method is approximately 15 Ω/sq, taking into consideration that the obtained result is an average value. [11]

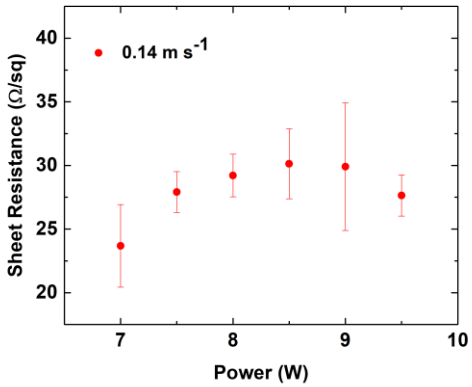

Figure 4.5 Optimized LIG sheet resistance

The structural nature of the optimized velocity samples at different laser powers was studied through Raman Spectroscopy and a summary of the results can be found on Figure 4.6. The most prominent features in the Raman spectra of graphene are called the G-band appearing at 1582 cm^{-1} and the G' band (also referred as 2D) at about 2700 cm^{-1}. The D band (disorder induced band) is seen at half the frequency of the G band. Due to the added forces from the interactions between layers of AB-stacked graphene as the number of graphene layers increases, the spectrum will change from that

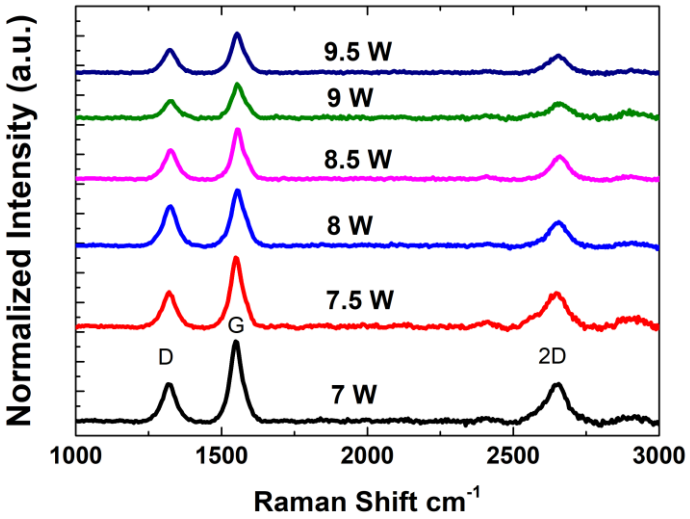

Figure 4.6 Raman spectrum of the samples with optimized velocity at different laser power

of single-layer graphene, namely a splitting of the G' (2D) peak into an increasing number of modes that can combine to give a wider, shorter, higher frequency peak. The G peak also experiences a smaller red shift from increased number of layers. [58] Also, the crystallite size of graphene is inversely proportional to G and D band intensities (I_D/I_G). [59] A higher laser power induces an observable

broadening of the 2D peak as well as an increased size of crystallite due to a diminished I_D/I_G. This proves that a higher conductivity is associated with graphene like features.

A third parameter, pulses per inch (PPI) was evaluated at a constant power and velocity to verify its influence on sheet resistance (Figure 4.7) Since no significant influence was verified, PPI was kept at the maximum (1000).

A full optimization included resolution tests (Figure 4.7) for the optimized sheet resistance. A linear calibration was obtained where y represents the obtained width and x the software width.

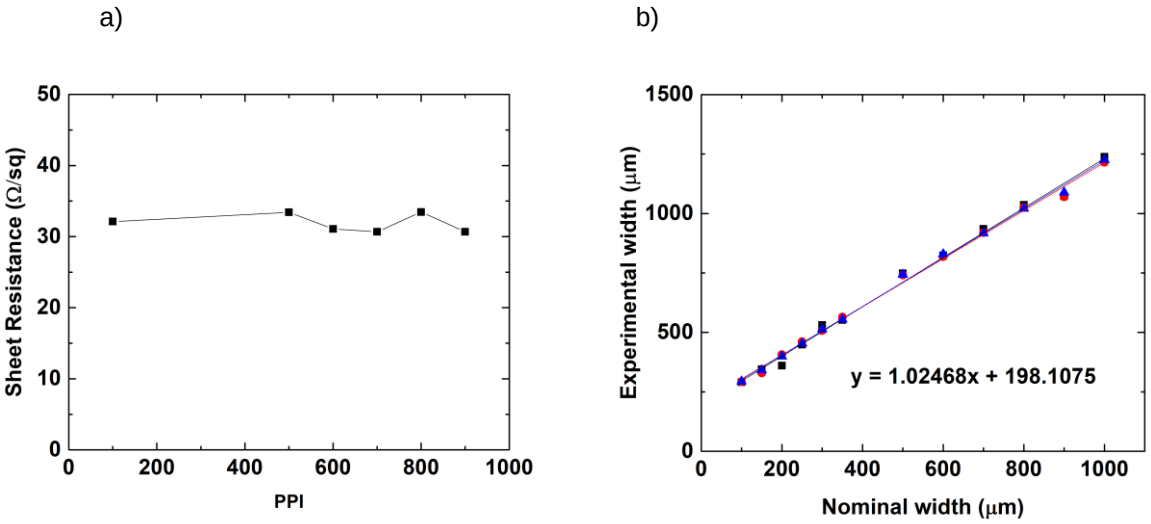

Figure 4.7 a) Influence of ppi on LIG sheet resistance b) Resolution tests and calibration of the optimized LIG

The same parameters were also tried on intermediate thickness (50 μm) PI but the best sheet resistance obtained (45 Ω/sq) was only achieved at an approximate velocity of 0.27 m s^{-1} (Figure 4.8). Heat dissipation is compromised due to the lower thickness and so the numbers of parameters that lead to laser induced graphene become more restricted, ablation occurs more often. A more effective induction is seen at higher power since a slightly higher velocity compensates for the compromised dissipation of heat.

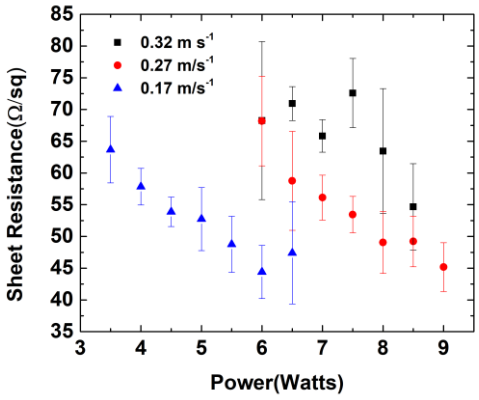

Figure 4.8 LIG optimized sheet resistance on intermediate thickness PI

4.1.2 Laser scribed graphene

As expected GO formed consistent films on PET after 48 hours. Even though an RT process is advantageous since it doesn't compromise PET integrity and hydrated films of graphene oxide could be considered as insulators, ambient conditions are variable, influence the drying process and introduce defects. Therefore, the resulting films were not homogeneous and contained many irregularities. Van der Wall forces actuating on the dispersed solution may have generated portions with higher concentrations of carbon while others may have suffered from a carbon deficit

The best results reported on literature for GO reduction via CO_2 laser irradiation were observed on free standing graphite oxide films obtained by vacuum filtration which present a better stability but are also much thicker.[6].The lowest measured sheet resistance was 180 Ω/sq but this result was not reproducible over a large area. The average sheet resistance obtained at 2.5 W for different velocities from 0.36 m s^{-1} up to 0.5 ms^{-1} was on the order of 10^3 Ω/sq. Although for increasing velocity (0.5 to 0.63 m s^{-1}) a considerable decrease was attained, there was not a clear tendency considering that the quality of the films is an important variable. The sheet resistance of the reduced graphene oxide was much higher than reported values on literature (80 Ω/sq) but this result was obtained with DVD LightScribe. [7] Considering the minimum laser power of the CO_2much higher than the LightScribe method which is limited to mW. Also, CO_2 lasers present longer wavelengths while every LightScribe system presents a shorter wavelength (~658 nm).

4.1.3 Microsupercapacitors with LIG electrodes

There are two kinds of supercapacitors that can be distinguished in literature. Electrical double-layer capacitors (EDLCs), which store charge by adsorption of electrolyte ions onto the surface of electrode materials. No redox reactions are required, so the response to changes in potential without the diffusion limitations is rapid.[60] Another common type of supercapacitors are pseudocapacitors in which, due to electron transfer between the electrolyte and the electrode, through fast Faradaic redox reactions charge is stored. [61] The behavior of interest in this study is the first one since charge is stored electrostatically so that an EDL at the electrolyte/gate interface is insured.

Cyclic voltammetry (CV) measurements and Electrochemical Impedance Spectroscopy (EIS) were performed on the above mentioned fabricated devices, namely on in plane graphene interdigital capacitors on PI. CV measurements importance relies on the indication of EDL capacitance achievement by presenting almost rectangular plots and no anodic/cathodic peaks. An approximation of electrolyte resistance to zero gives rise to a rectangular shape whereas high electrolyte resistances result in a more elongated shape on cyclic voltammograms [61] The EIS study of the capacitive behavior with frequency also provides valuable information, namely the maximum frequency at which a capacitive behavior can be found. Also, equivalent circuit models (ECM) are pertinent where it is intended to study the behavior of the electrochemical cell, as it allows to quantify crucial parameters, such as bulk resistivity (ρ), ionic conductivity (σ_i), bulk capacitance (C_b) and EDL capacitance (C_{DL}) associated to the used electrolyte.

4.1.3.1 Cyclic Voltammetry of the CHE capacitor

CV measurements of the CHE capacitor at different scan rates from -2 to 2 V were performed to evaluate the influence of graphene electrodes. At the lowest scan rate, anodic and cathodic peaks are still identifiable probably related to electrolyte hydrolysis .[17]. Anodic and cathodic peaks at fast scan rates disappear due to the chemical inertness of graphene and a probable pseudocapacitance effect, meaning that reversible redox reaction could be taking place but at such a high rate that become undetectable, as it can be observed on Figure 4.9.

a) b)

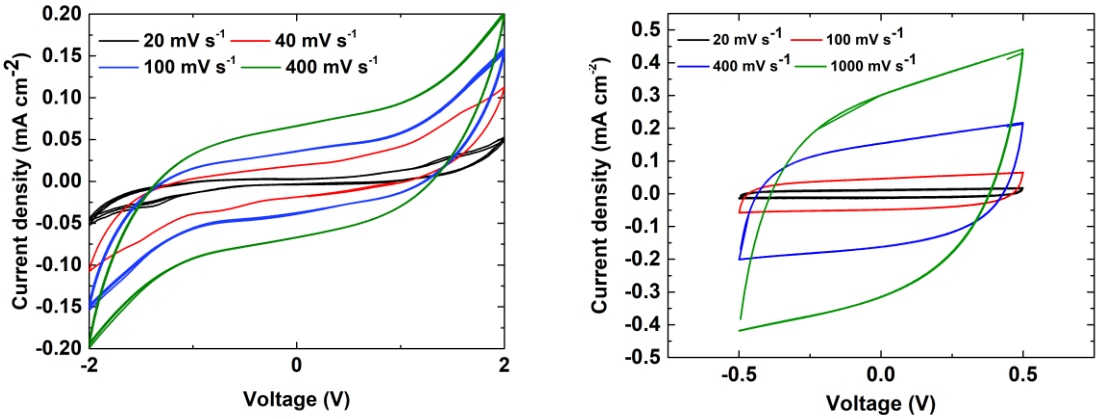

Figure 4.9 CV measurements of CHE capacitor a) from -2 to 2 V at different scan rates b) from -0.5 to 0.5 V at different scan rates

A pseudo-rectangular shape, characteristic of the electric double layer formation can be observed within voltages where no redox reactions (-0.5 V to 0.5 V) take place. This also suggests that the possible remaining content of oxygen and nitrogen present on LIG do not chemically react with the electrolyte because no cathodic or anodic peaks are observed even at the lowest scan rate as it can be observed from Figure 4.9. [11] Also, a simple conclusion is that to restrict faradaic currents to negligible values, drain voltages in transistors need to be limited to small values like in the present case 0.5 V.[30]

4.1.3.2 EIS of the CHE capacitor

According with the depicted EIS measurements on Figure 4.10, as expected for frequencies above 100 Hz and a phase angle between current and voltage higher than -45º, a highly resistive behavior is observed due to ionic relaxation. Even at low frequencies, a plateau of the phase angle is reached at 80º suggesting a non-ideal capacitive behavior. At 100 mHz, a slightly higher specific capacitance than the previously reported is reached (up to 47 µF cm^{-2}), however at a phase angle corresponding to -45º between 1 and 2 Hz capacitance decreases to 0.15 µF cm^{-2}. Ionic relaxation may be achieved at lower frequencies because these electrodes present a high superficial area and with an increased frequency the electrolyte is not able to respond to an increased charge as at low frequencies

where high capacitances are achieved. A non-ideal behavior can also be observed with the Nyquist plot (Figure 4.10) where at low frequencies, a vertical line should be associated with a phase margin of 90º which is never achieved, although an increase in verticality compared with previously used electrodes can be seen.[17]

The Dasgupta et al. ECM model (Figure 4.10) presents a good fit (1.43 ×10^3 goodness of fit) where it includes a resistance (R_{ext}) that is associated to contact resistances, in series with an RC circuit and a constant phase element (CPE). [17], [62] Regarding the RC circuit, R_b embodies the bulk resistance and C_b the electrolyte bulk capacitance which is associated to the dipolar relaxation of the electrolyte solvent molecules. Double layer capacitance (C_{dl}) was calculated using Equations 5 and 6 where Υ_0 is the capacitance associated to CPE, α is a constant between 0 and 1 that determines how non-ideal the capacitor behaves, l is the thickness of the electrolyte membrane and A is the surface area. The results obtained through fitting result in a much higher bulk and external resistance and so a considerable reduction in ionic mobility is observed (4×10^{-5} S cm^{-1}) as well as an increase in double layer capacitance (34 µF cm^{-2}) when compared with the reported results. The α constant also presents a higher value of 0.89.[17]

$$C_{dl} = \left[\Upsilon_0 R_{ext}^{-(\alpha-1)}\right]^{1/\alpha} \quad (5)$$

$$\sigma_i = \frac{l}{R_b A} \quad (6)$$

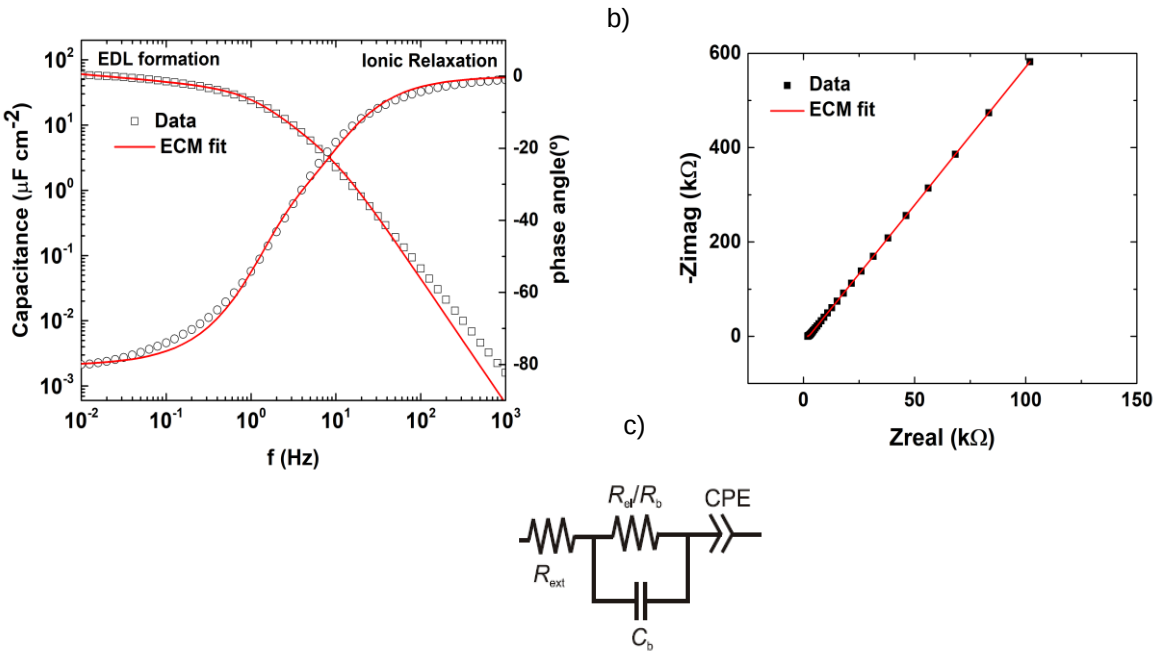

Figure 4.10 a) Capacitance and phase angle versus frequency plots of the CHE capacitor b) Nyquist plot of the CHE capacitor c) ECM model adapted from [62]

4.1.3.3 Cyclic voltammetry of the TMAHP capacitor

Minor cathodic and anodic peaks can be visualized at low scan rates on the cyclic voltammogram of TMAHP from -2 to 2 V Once again cathodic and anodic peaks are not visible at high scan rates, probably due to the reversibility of the reactions taking place The less rectangular elongated shape could be associated with an in-series resistance of the device associated with some pseudocapacitance.

a) b)

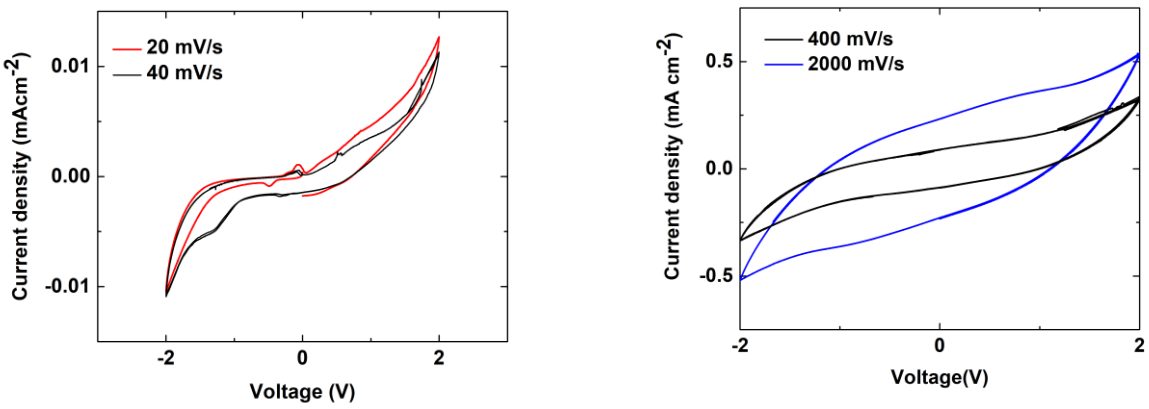

Figure 4.11 CV measurements of the TMAHP capacitors from -2 to 2 V a) at low scan rates b) at high scan rates

4.1.3.4 EIS of the TMAHP capacitor

Impedance spectroscopy on porous materials regularly results in data that cannot be modeled with standard circuit components. The represented ECM (Figure 4.12) consists of two in series RC circuits based on Randles ECM. The RC circuit once again is composed of a resistance (charge transfer resistance) in parallel with a capacitor whose non-ideality is presented through a CPE. The main difference between the obtained RC results is seen on the α constants associated with the CPE. The first α constant of 0.99 is associated with an ideal capacitor and the second one with a value of 0.5 is associated with Warburg impedance accounting for a considerable ion diffusion within the separator (titanium 60l), related to molecule difficulty in reaching a bare electrode. [63] Hence, two different double layer capacitances arise, a double layer capacitance of 280 µF cm^{-2} and 120 µF cm^{-2}, respectively. At 0.01 Hz the calculated capacitance was 220 µF cm^{-2}, within the same order of the calculated double layer capacitance. Regarding the goodness of fit of 1.53×10^{-3}, this model is a good approximation although at high frequencies a fitness deterioration can be observed. Considering the phase angle peak at -35º, it is possible to conclude that there is a high solution resistance. Above 100 Hz, the resistive behavior becomes dominant with the phase angle approaching 0º. The Nyquist plot present on Figure 4.12 is typical of an RC circuit meaning that the that it deviates from a straight line and a common semicircle is found. high solution resistance can be confirmed due to the radius size of the semicircle.

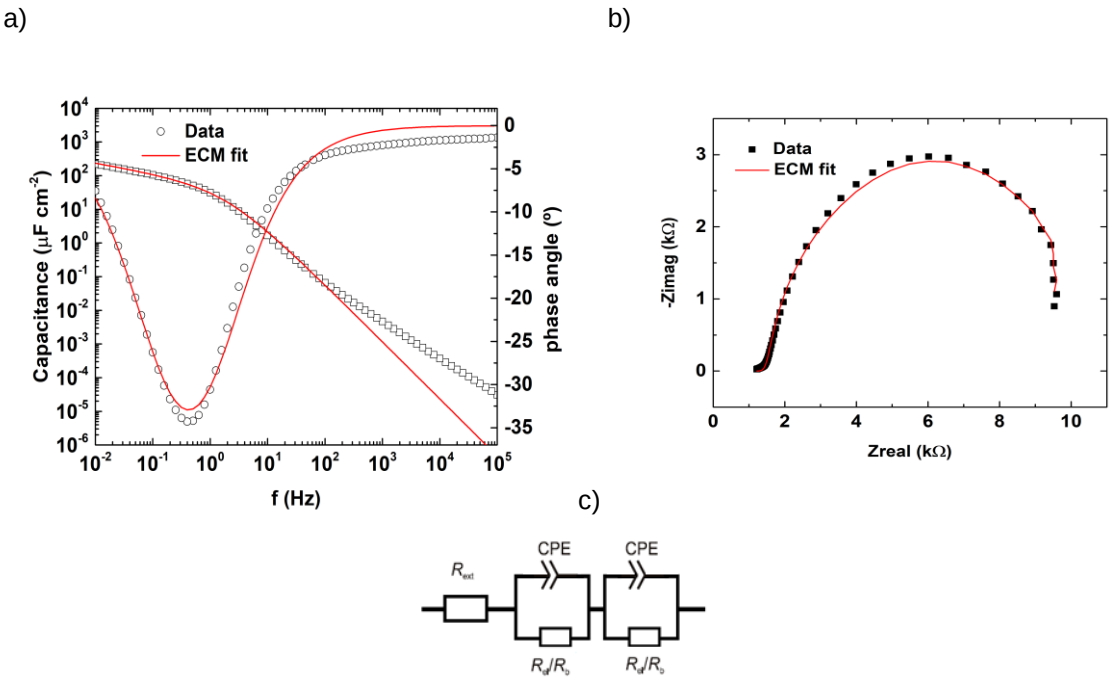

Figure 4.12 a) Capacitance and phase angle versus frequency plots of the TMAHP capacitor b) Nyquist plot of the TMAHP capacitor from 10^{-2} to 10^{5} Hz c) ECM model adapted from [63]

4.1.3.5 Cyclic voltammetry with the semiconductor layer

Cyclic voltammetry with the semiconductor layer, namely a screen-printed layer of the ZnO dispersion in ethyl cellulose, was performed so that possible redox reactions between the ink and the electrolyte could be identified. The existence of anodic and/or cathodic peaks also reveals important information about the ink permeability. The ink impermeability plays a major role because it determines the double layer formation at the semiconductor/electrolyte interface.

According with depicted voltammograms (Figure 4.13) on the ZnO ink is more impermeable to CHE than to the TMAHP capacitor. As it can be observed on the voltammogram on the left, a considerable decrease in current density is observed and the occurrence of redox reactions is not detectable due to the resolution limitation of the device, since the noise could superimpose the redox signal. Even at 400 m s^{-}1 A possible explanation for the TMAHP permeability could be formation of hydrogen bonds with oxygen that act as shallow donors as mentioned above.[42] Therefore it can be said that in case of the CHE transistors two parallel layers of positive and negative layers which result in charge accumulation while in the case of the TMAHP transistors, a reversible doping of the semiconductor layer occurs due to redox reactions taking place.

a) b)

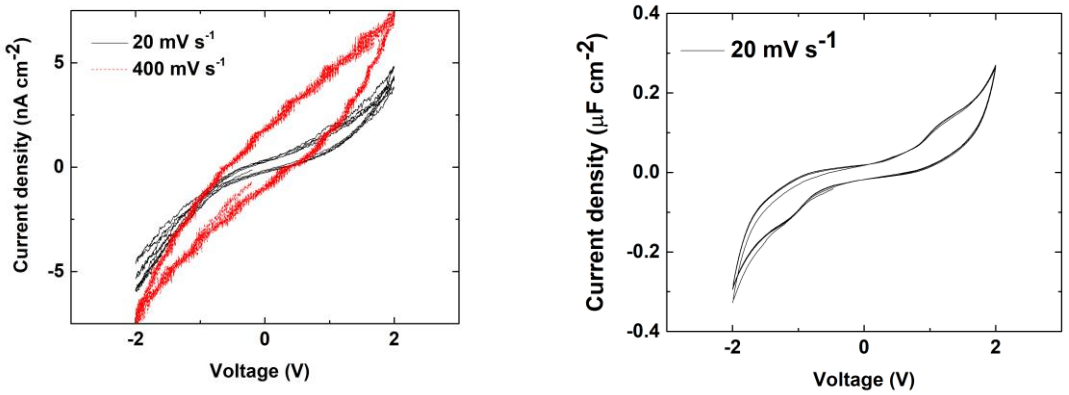

Figure 4.13 CV measurements from -2 to 2 V of the capacitors with the semiconductor layer a) CHE capacitor at different scan rates b) TMAHP capacitor at 20 mV s^{-1} scan rate

4.2 Electrical characterization of the EGTs

The previous chapters were essential to understand all the fundamental properties of the used layers in the devices under study. Now, the focus in these next subsections will be on the electrical characterization of the ZnO NPs EGTs and the electrolyte influence. The interdigital electrodes were fabricated with the limit resolution of 198 µm, and so considering the average width of the screen-printed layer (68095 µm)[54], an approximate W/L of 365.5 was obtained and the same ratio was used on all characterizations.

4.2.1 CHE EGTs

Figure 4.14 shows two transfer curves of CHE EGTs, in the saturation regime. As has been reported, the major drawbacks of the EGTs are linked to the large leakage gate current (I_{GS}). These can be confirmed by the transfer characteristics and its influence on devices I_{DS}, particularly at low and high V_{GS}, determining the off current (I_{Off}) and limiting the maximum on current (I_{On}), respectively. Regarding the double sweep measurements, the devices show an anti-clock hysteresis related to slow ion migration. Ideally, a voltage sweep back, when reaching a value below V_{on}, would result in the collapse of the double layer. An analysis of the transfer characteristics leads to the conclusion that a complete OFF state is never reached due to the entrapment of charges on the semiconductor-electrolyte interface. Also, due the to the room temperature processing of the ZnO NPs dispersions, a significant fraction of agglomerates that are at several times larger than the primary particle size and thereby produce a large enough roughness between the transistor channel and the gate insulator and so the created charge traps hinder charge transfer.[62]

The saturation mobility (μ_{Sat}) of the devices, since they are working in saturation regime was determined through Equation 7 where the numerator represents transconductance (g_m), I_D, represents the drain current, V_G the gate voltage and C_i the capacitance of the dielectric layer which in this case corresponds to the double layer capacitance previously calculated (34 µF cm^{-2}).

$$\mu_{sat} = \frac{\left(\frac{d\sqrt{I_D}}{dV_G}\right)^2}{\frac{1}{2}C_i\frac{W}{L}} \quad (7)$$

A summary of the calculated parameters is present on the obtained values of saturation mobility indicate also ineffective gating since mobilities on the order of 10^{-3} are lower than the intrinsic mobility of the semiconductor. Additionally, contact resistance can also have an influence on the low μ_{Sat} as contact between channel and S/D is made by contact points (nanoparticles) instead of a continuous surface.

The inverse of the maximum slope of the transfer characteristic, the subthreshold swing (S_s) was also calculated. This parameter indicates the necessary V_G to increase I_D by one decade and values between 0.1 and 0.3 indicate low power consumption. [20]

Table 4.1 Summary of the electrical characterization of the CHE EGTs

V_{DS}	V_{ON} (V)	ON/OFF	S_s (Vdec^{-1})	g_m (S)	μ_{Sat} (cm^2 (Vs)$^{-1}$)
2	2.9	10^2	0.41	4.7×10 $^{-5}$	7.8 x 10^{-3}

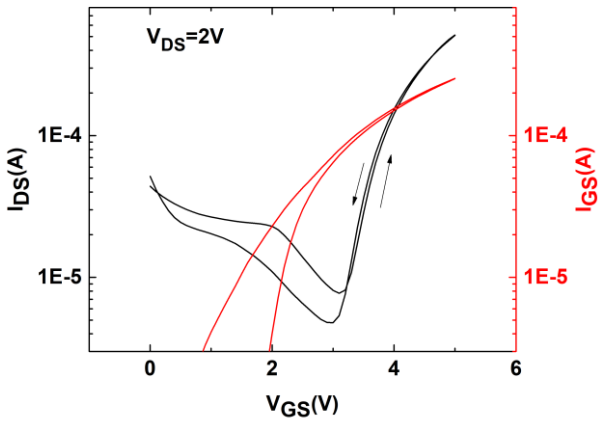

Figure 4.14 I_{DS}–V_{GS} transfer characteristics, in saturation regime, as well as the behavior of IGS, for the CHE EGT

The output characteristics are present on Figure 4.15. The flatness of the curves indicates that depletion occurs close to the drain electrode, even if not fully. For higher V_{GS}, depletion can be impaired since the curves become less flat. For low V_{DS} some current crowding can be found, revealing possible problems at the source-drain contacts. Also, the decreasing separation between I_{DS}-V_{DS} for increasing V_{GS} curves suggests mobility degradation.[20]

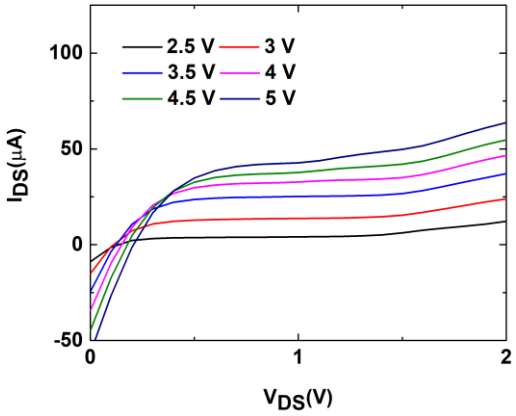

Figure 4.15 the drain current–drain voltage (I_{DS}-V_{DS}) output characteristics of the CHE transistor at different V_{GS}

4.2.2 TMAHP EGT

The transfer curve of the TMAHP transistor is depicted on Figure 4.16. As it can be observed, the hysteresis enhancement is significative due to the predominantly resistive behavior observed by EIS analysis and due to the reversible redox reactions, that can be observed at low scan rates in CV measurements. These reactions may be simultaneously responsible for the reversible doping of the semiconductor layer and ineffective gating, since the EDL formation at the electrolyte-gate interface may be compromised. The summary of the obtained results depicted on Table 4.2 Summary of the TMAHP EGT electrical characterization Table 4.2 indicates, especially saturation mobility confirms an ineffective gating due to the afore mentioned reasons.

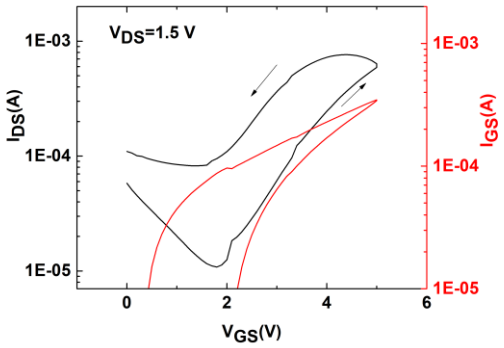

Figure 4.16 I_{DS}–V_{GS} transfer characteristic, in saturation regime of the TMAHP EGT

Table 4.2 Summary of the TMAHP EGT electrical characterization

V_{DS}	V_T (V)	ON/OFF	g_m (S)	μ_{Sat} $(cm^2\ (Vs)^{-1})$
1.5	2.3	8.3×10^2	1×10^{-4}	3×10^{-3}

5 CONCLUSION AND FUTURE PERSPECTIVES

In the present work, some main objectives were achieved namely the development of conductive carbonized structures by laser irradiation of polyamide which are patternable and are highly reproducible. It was possible to conclude that laser power and velocity highly influence the obtained carbonized material, not only morphologically, with changes in thickness and porosity, but chemically, preventing oxidation and rearrangements of the carbon structure. The optimized sheet resistance (24 Ω/sq) was associated graphene like features, a reduction of the crystallite size and a higher 2D peak as it can be seen by Raman Spectroscopy. Also, in the present work, the direct writing by polymer carbonization was a much more reliable method than graphene oxide reduction by laser irradiation. In the future, techniques that prevent inhomogeneity should be employed such as screen printing or inkjet printing. A significant cost reduction of these patternable electrodes can be achieved by simplifying the traditional Hummers method used for graphite oxidation and by using cheaper substrates like PET. In both techniques, for mass production to take place, smaller areas need to be patterned and to accomplish that lasers with shorter wavelengths enabling higher resolutions should be employed. Furthermore, transfer methods of LIG should be studied for substrates where biosensing or transparency are required.

Another goal was the improvement of double layer capacitance through the application of LIG electrodes. The CV measurements of the CHE capacitor with a voltage range between -0.5 V and 0.5 V where faradaic currents are restricted indicate a supercapacitor behavior which is associated with the formation of EDL and hence a high reversible polarizability of the electrolyte can be achieved On the other hand due to the structure of the fabricated electrodes which present an increased superficial area and also high porosity, a decrease in the capacitive behavior is observed at higher frequencies on EIS can be observed. Two reasons could explain this decrease, namely an increase in the superficial area and elevated porosity. An increase in the superficial area results in an increase of the superficial charge which may compromise the electrolyte response at higher frequencies. Regarding the porosity of the presented material, diffusion reactions may also be taking place and so the LIG behavior as a blocking electrode is not confirmed. CV measurements with the TMAHP capacitor resulted in voltammograms with a less rectangular more elongated shape which is associated with in series resistance. CV measurements also indicated a predominance of pseudocapacitance, meaning that the origin of the capacitive behavior relies on fast redox reaction. The high resistance of the electrolyte embedded in the separator membrane was confirmed through EIS analysis where the maximum phase angle achieved was -35º.

Regarding EGTs, a proof of concept was achieved although a highly ineffective gating is present. Several factors compromise EGT performance, such as high large roughness at the channel-electrolyte interface which may have induced charge traps that hinder charge transfer from drain to source. Low mobilities on the order of 10^{-3} are a result of an inhomogeneous field at the channel-electrolyte interface. Considering that a room temperature ink was applied, several agglomerates may appear and so a more effective surface functionalization of the ink needs to be considered. [62] Rapid laser annealing, for example, should be considered as an alternative process for surface functionalization.

Overall, in the future complex electronic circuits could be patterned via laser irradiation since in the present work the direct carbonization of electrodes in PI originated several components such as resistances, capacitors and even transistors. The facile fabrication and design provided with this method is a step towards customizable and printable electronics.

6 BIBLIOGRAPHY

[1] P. R. A, A. C. B, and C. G. C, “The Potential of Printed Electronics and Personal Fabrication in Driving the Internet of Things,” vol. 1, no. 1, 2015.

[2] J. Perelaer *et al.*, “Printed electronics: the challenges involved in printing devices, interconnects, and contacts based on inorganic materials,” *J. Mater. Chem.*, vol. 20, no. 39, p. 8446, 2010.

[3] Y. S. Rim, S. H. Bae, H. Chen, N. De Marco, and Y. Yang, “Recent Progress in Materials and Devices toward Printable and Flexible Sensors,” *Adv. Mater.*, vol. 28, no. 22, pp. 4415–4440, 2016.

[4] S. Khan, L. Lorenzelli, R. S. Dahiya, and S. Member, “Technologies for Printing Sensors and Electronics Over Large Flexible Substrates : A Review,” vol. 15, no. 6, pp. 3164–3185, 2015.

[5] M. Magliulo *et al.*, “Printable and flexible electronics: from TFTs to bioelectronic devices,” *J. Mater. Chem. C*, vol. 3, no. 48, pp. 12347–12363, 2015.

[6] W. Gao *et al.*, “Direct laser writing of micro-supercapacitors on hydrated graphite oxide films,” *Nat. Nanotechnol.*, vol. 6, no. 8, pp. 496–500, Jul. 2011.

[7] V. Strong *et al.*, “Patterning and electronic tuning of laser scribed graphene for flexible all-carbon devices,” *ACS Nano*, vol. 6, no. 2, pp. 1395–1403, 2012.

[8] M. F. El-Kady and R. B. Kaner, “Scalable fabrication of high-power graphene micro-supercapacitors for flexible and on-chip energy storage.,” *Nat. Commun.*, vol. 4, p. 1475, 2013.

[9] M. A. Mohammad *et al.*, “Tunable graphene oxide reduction and graphene patterning at room temperature on arbitrary substrates,” *Carbon N. Y.*, vol. 109, pp. 173–181, 2016.

[10] I. I. Bobrinetskiy, A. V Emelianov, S. A. Smagulova, I. A. Komarov, N. Otero, and P. M. Romero, “Laser direct 3D patterning and reduction of graphene oxide film on polymer substrate,” *Mater. Lett.*, vol. 187, no. October 2016, pp. 20–23, 2017.

[11] J. Lin *et al.*, “Laser-induced porous graphene films from commercial polymers,” *Nat. Commun.*, vol. 5, no. 5714, pp. 1–8, 2014.

[12] F. Clerici *et al.*, “In situ MoS2-decoration of laser induced graphene as flexible supercapacitor electrodes,” 2016.

[13] Z. Peng, J. Lin, R. Ye, E. L. G. Samuel, and J. M. Tour, “Flexible and Stackable Laser Induced Graphene Supercapacitors,” 2015.

[14] L. Li *et al.*, “High-Performance Pseudocapacitive Microsupercapacitors from Laser-Induced Graphene,” *Adv. Mater.*, vol. 28, no. 5, pp. 838–845, Feb. 2016.

[15] S. H. Kim *et al.*, “Electrolyte-Gated Transistors for Organic and Printed Electronics,” *Adv. Mater.*, vol. 25, no. 13, pp. 1822–1846, Apr. 2013.

[16] E. Bandiello, M. Sessolo, and H. J. Bolink, “Aqueous electrolyte-gated ZnO transistors for environmental and biological sensing †,” *J. Mater. Chem. C Mater. Opt. Electron. devices*, vol. 2, pp. 10277–10281, 2014.

[17] I. Cunha, R. Barras, P. Grey, D. Gaspar, E. Fortunato, and R. Martins, “Reusable Cellulose-Based Hydrogel Sticker Film Applied as Gate Dielectric in Paper Electrolyte-Gated Transistors,” vol. 1606755, 2017.

[18] M. Halper and J. Ellenbogen, “Supercapacitors: A brief overview,” *Rep. No. MP 05W0000272, …*, no. March, p. Report No. MP 05W0000272, 1-29, 2006.

[19] E. Fortunato, P. Barquinha, and R. Martins, “Oxide Semiconductor Thin-Film Transistors : A Review of Recent Advances,” pp. 2945–2986, 2012.

[20] P. Barquinha, “Transparent Oxide Thin-Film Transistors :,” Faculdade de Ciências e Tecnologias, 2010.

[21] J. Bardeen and W. H. Brattain, “Transistor, a semiconductor triode,” *Proc. IEEE*, vol. 86, no. 1, pp. 29–30, 1998.

[22] S. R. C. Vivekchand, C. S. Rout, K. S. Subrahmanyam, A. Govindaraj, and C. N. R. Rao, “Graphene-based electrochemical supercapacitors,” vol. 120, no. 1, pp. 9–13, 2008.

[23] K. S. Novoselov, V. I. Fal, L. Colombo, P. R. Gellert, M. G. Schwab, and K. Kim, “REVIEW A roadmap for graphene,” *Nature*, vol. 490, no. 7419, pp. 192–200, 2012.

[24] W. Choi *et al.*, “Synthesis of Graphene and Its Applications : A Review Synthesis of Graphene and Its Applications : A Review,” vol. 8436, no. August, 2017.

[25] M. J. Allen, V. C. Tung, and R. B. Kaner, “Honeycomb Carbon : A Review of Graphene,” pp. 132–145, 2010.

[26] S. Alam, B. Nizam, and U. Maksudul, “Synthesis of graphene,” *Int. Nano Lett.*, vol. 6, no. 2, pp. 65–83, 2016.

[27] R. L. Hoffman, B. J. Norris, and J. F. Wager, “ZnO-based transparent thin-film transistors,” *Appl. Phys. Lett.*, vol. 82, no. 5, pp. 733–735, 2003.

[28] P. F. Carcia, R. S. McLean, M. H. Reilly, and G. Nunes, “Transparent ZnO thin-film transistor fabricated by rf magnetron sputtering,” *Appl. Phys. Lett.*, vol. 82, no. 7, pp. 1117–1119, 2003.

[29] S. Masuda, K. Kitamura, Y. Okumura, S. Miyatake, H. Tabata, and T. Kawai, “Transparent thin film transistors using ZnO as an active channel layer and their electrical properties,” *J. Appl. Phys.*, vol. 93, no. 3, pp. 1624–1630, 2003.

[30] R. Kruk *et al.*, “Environmentally Stable Operation of Electrochemically-Gated Zinc Oxide Nanowire ... High-Speed , Low-Voltage , and Environmentally Stable Operation of Electrochemically-Gated Zinc Oxide Nanowire Field-Effect Transistors,” no. August, 2017.

[31] E. Fortunato *et al.*, “High field-effect mobility zinc oxide thin film transistors produced at room temperature,” vol. 340, pp. 806–809, 2004.

[32] E. M. C. Fortunato *et al.*, “Wide-bandgap high-mobility ZnO thin-film transistors produced at room temperature Wide-bandgap high-mobility ZnO thin-film transistors produced at room temperature,” vol. 2541, no. 2004, pp. 98–101, 2005.

[33] A. C. M. B. G. Pimentel, A. M. F. Gonçalves, A. J. S. Marques, L. M. N. Pereira, and R. F. P. Martins, “Fully Transparent ZnO Thin-Film Transistor Produced at Room Temperature **,” no. 5, 2005.

[34] B. J. Norris, J. Anderson, J. F. Wager, and D. A. Keszler, “Spin-coated zinc oxide transparent,” vol. 105, 2003.

[35] J. Schneider, R. C. Hoffmann, O. Soffke, W. Jaegermann, A. Issanin, and A. Klyszcz, “A Printed and Flexible Field-Effect Transistor Device with Nanoscale Zinc Oxide as Active Semiconductor

Material **," pp. 3383–3387, 2008.

[36] H. Bong *et al.*, "High-mobility low-temperature ZnO transistors with low-voltage operation High-mobility low-temperature ZnO transistors with low-voltage operation," vol. 192115, no. 2010, pp. 3–6, 2016.

[37] J. Smith *et al.*, "High-Performance Zinc Oxide Transistors and Circuits Fabricated by Spray Pyrolysis in Ambient Atmosphere," pp. 2226–2231, 2009.

[38] K. Hong, S. H. Kim, K. H. Lee, and C. D. Frisbie, "Printed, sub-2V ZnO electrolyte gated transistors and inverters on plastic," *Adv. Mater.*, vol. 25, no. 25, pp. 3413–3418, 2013.

[39] T. Jesionowski, "Zinc Oxide — From Synthesis to Application: A Review," pp. 2833–2881, 2014.

[40] Ü. Özgür *et al.*, "A comprehensive review of ZnO materials and devices APPLIED PHYSICS REVIEWS A comprehensive review of ZnO materials and devices," vol. 41301, 2005.

[41] A. Janotti and C. G. Van De Walle, "Fundamentals of zinc oxide as a," 2009.

[42] C. G. Van De Walle, "Hydrogen as a Cause of Doping in Zinc Oxide," vol. 85, no. 1, pp. 0–3, 2000.

[43] M. D. McCluskey, M. C. Tarun, and S. T. Teklemichael, "Hydrogen in oxide semiconductors," *J. Mater. Res.*, vol. 27, no. 17, pp. 2190–2198, 2012.

[44] T. Q. Trung and N. E. Lee, "Recent Progress on Stretchable Electronic Devices with Intrinsically Stretchable Components," *Adv. Mater.*, vol. 29, no. 3, 2017.

[45] Y. Zhang *et al.*, "Direct imprinting of microcircuits on graphene oxides film by femtosecond laser reduction," *Nano Today*, vol. 5, no. 1, pp. 15–20, 2010.

[46] Z. Wei *et al.*, "Nanoscale Tunable Reduction of Graphene Oxide for Graphene Electronics," *Science (80-.).*, vol. 328, no. 5984, 2010.

[47] Y. Chen *et al.*, "Enhanced electrochemical performance of laser scribed graphene films decorated with manganese dioxide nanoparticles," *J. Mater. Sci. Mater. Electron.*, vol. 27, no. 3, pp. 2564–2573, Mar. 2016.

[48] V. Strong *et al.*, "Patterning and Electronic Tuning of Laser Scribed Graphene for Flexible All-Carbon Devices," *ACS Nano*, vol. 6, no. 2, pp. 1395–1403, Feb. 2012.

[49] R.-Z. Li *et al.*, "High-rate in-plane micro-supercapacitors scribed onto photo paper using in situ femtolaser-reduced graphene oxide/Au nanoparticle microelectrodes," *Energy Environ. Sci.*, vol. 9, no. 4, pp. 1458–1467, 2016.

[50] V. A. Online *et al.*, "Environmental Science scribed onto photo paper using in situ," pp. 1458–1467, 2016.

[51] M. Schumann, R. Sauerbrey, and M. C. Smayling, "Permanent increase of the electrical conductivity of polymers induced by ultraviolet laser radiation," *Appl. Phys. Lett.*, vol. 58, no. 4, pp. 428–430, 1991.

[52] S. Byun, H. Lim, G. Shin, T. Han, S. H. Oh, and J. Ahn, "Supporting Information Graphenes Converted from Polymers," pp. 1–11, 2011.

[53] A. Lamberti, F. Clerici, M. Fontana, and L. Scaltrito, "A Highly Stretchable Supercapacitor Using Laser-Induced Graphene Electrodes onto Elastomeric Substrate," pp. 1–6, 2016.

[54] T. Carvalho, "Field-Effect Transistors Based on Zinc Oxide Nanoparticles," Faculdade de

Cinências e Tecnologias, 2015.

[55] K. Inukai, Y. Takahashi, K. Ri, and W. Shin, “Rheological analysis of ceramic pastes with ethyl cellulose for screen-printing,” *Ceram. Int.*, vol. 41, no. 4, pp. 5959–5966, 2015.

[56] M. Fekete, W. Riedel, F. Patti, and L. Spiccia, “Photoelectrochemical water oxidation by screen printed ZnO nanoparticle fi lms : e ff ect of pH on catalytic activity and stability †,” pp. 7585–7593, 2014.

[57] J. Su and A. C. Lua, “Effects of carbonisation atmosphere on the structural characteristics and transport properties of carbon membranes prepared from Kapton?? polyimide,” *J. Memb. Sci.*, vol. 305, no. 1–2, pp. 263–270, 2007.

[58] I. Childres, L. Jauregui, W. Park, H. Cao, and Y. Chen, “Raman Spectroscopy of Graphene and Related Materials,” *New Dev. Phot. Mater. Res.*, pp. 1–20, 2013.

[59] L. G. Caņado *et al.*, “General equation for the determination of the crystallite size la of nanographite by Raman spectroscopy,” *Appl. Phys. Lett.*, vol. 88, no. 16, pp. 1–4, 2006.

[60] P. Simon, Y. Gogotsi, and B. Dunn, “Where Do Batteries End and Supercapacitors Begin?,” *Science (80-.).*, vol. 343, no. 6176, pp. 1210–1211, 2014.

[61] W. G. Pell and B. E. Conway, “Analysis of power limitations at porous supercapacitor electrodes under cyclic voltammetry modulation and dc charge,” *J. Power Sources*, vol. 96, no. 1, pp. 57–67, 2001.

[62] S. Dasgupta *et al.*, “Printed and electrochemically gated, high-mobility, inorganic oxide nanoparticle FETs and their suitability for high-frequency applications,” *Adv. Funct. Mater.*, vol. 22, no. 23, pp. 4909–4919, 2012.

[63] “Basics of EIS: Electrochemical Research-Impedance.” [Online]. Available: https://www.gamry.com/application-notes/EIS/basics-of-electrochemical-impedance-spectroscopy/. [Accessed: 05-Oct-2017].

[64] C. Phillips, D. Beynon, S. Hamblyn, G. Davies, D. Gethin, and T. Claypole, “A Study of the Abrasion of Squeegees Used in Screen Printing and Its Effect on Performance with Application in Printed Electronics,” *Coatings*, vol. 4, no. 2, pp. 356–379, 2014.

[65] A. Hunt *et al.*, “Modulation of the band gap of graphene oxide: The role of AA-stacking,” *Carbon N. Y.*, vol. 66, pp. 539–546, 2014.